Journal of Magnetic Resonance 195 (2008) 211–218

Contents lists available at ScienceDirect

Journal of Magnetic Resonance

journal homepage: www.elsevier.com/locate/jmr

Stabilization of alternating TR steady-state free precession sequences

Hsu-Lei Lee *, Krishna S. Nayak

Ming Hsieh Department of Electrical Engineering, University of Southern California, 3740 McClintock Avenue EEB 412, Los Angeles, CA 90007, USA

ARTICLE INFO

Article history:
Received 22 May 2008
Revised 17 September 2008
Available online 23 September 2008

Keywords:
Alternating repetition time
Balanced SSFP
Initial preparation

ABSTRACT

Alternating TR steady-state free precession (ATR SSFP) has been proposed as a method to achieve a favorable frequency response compared to that of conventional balanced SSFP. ATR SSFP, much like conventional SSFP, exhibits oscillatory transient signal behavior that can degrade image quality. Thus an efficient preparation scheme is desired in order to actively reduce this initial signal fluctuation. Using an approach similar to that of Le Roux [Simplified model and stabilization of SSFP sequences, J. Magn. Resonan. 163 (1) (2003) 23–37], we construct a mathematical model for ATR SSFP sequences and show a Fourier relation between the separated odd and even terms of the RF flip angle increment sequence during an initial preparation, and the resulting oscillatory residues. A weighted Kaiser–Bessel windowed ramp can be used to design preparation schemes for arbitrary TR_1, TR_2, and RF phase cycling combinations. Optimized Kaiser–Bessel windowed ramp preparations for wideband SSFP and fat-suppressed ATR SSFP imaging are tested in phantoms. The results show substantially reduced transient signal oscillation with this new initial preparation method.

© 2008 Elsevier Inc. All rights reserved.

1. Introduction

In balanced steady-state free precession (SSFP) MR imaging [1], both the magnetization and the received signal oscillates during the approach to steady state. The fluctuating signal creates a non-smooth weighting in k-space that results in substantial image artifact [2,3]. The duration of these transient oscillations is on the order of the tissue T_1 relaxation time. It is possible to simply wait for the steady-state to be reached, however, this compromises the effectiveness of magnetization preparation schemes (e.g. fat saturation or inversion recovery) that are essential in many SSFP applications. Efficient initial preparation schemes are critical for the broad use of SSFP sequences. Simple methods such as $\alpha/2$-TR/2 preparation [2] can quickly align the magnetization in the direction of its steady state, but only for a limited off-resonance range.

To achieve good transient oscillation suppression for a wider range of frequencies, more elaborate methods were proposed. For conventional balanced SSFP, Le Roux [4] used the SU_2 formalism [5–7] to develop a simplified model for transient signal behavior, and to demonstrate a Fourier relation between RF flip angle increments and the resulting oscillatory residues. A Kaiser–Bessel windowed ramp preparation method was proposed to minimize oscillatory transients [4]. This approach has been widely adopted, and is the current method-of-choice for reducing transient artifacts in conventional balanced SSFP imaging. Initial preparation schemes based on the Shinnar–Le Roux (SLR) algorithm have also been proposed [8,9], which rely on sequences of RF pulses that accurately generate the steady-state frequency response by magnitude-scaling and direction-selection. In addition to its design complexity, this method is sensitive to B_1 variation.

Alternating TR SSFP has been recently proposed as a way to achieve a favorable frequency response compared to conventional SSFP. In the case of fat-suppressed ATR (FS-ATR) SSFP [10], a wide stopband is achieved capable of suppressing fat in the steady state. In the case of wideband SSFP [11], the spacing between nulls in the frequency response can be increased which mitigates banding artifacts for a given TR. Single-tip preparation was previously used for alternating TR SSFP sequences [10]. Paired Kaiser–Bessel design has been recently shown to have a performance comparable to optimum SLR design when there is a sufficient number of preparation cycles [12].

In this work, we adapt the SU_2 formalism approach to build a mathematical model for alternating TR SSFP signal behavior. This model provides justification for the use of Kaiser–Bessel windowed ramps, and a method for optimizing these ramps. Optimized initial preparation sequences for fat suppressed ATR SSFP and wideband SSFP are validated in simulation and phantom studies. We also describe a preparation scheme that can be applied to any alternating TR sequence with any RF phase cycling scheme.

2. Theory

In alternating TR SSFP (Fig. 1), two repetition times TR_1 and TR_2 are used, and the phases of RF excitation in the two TRs are 0 and $(\pi + \varphi)$, respectively [10,11]. A full cycle of the steady state contains two excitations and two periods of free precession and relaxation. Unlike conventional SSFP, the steady-state magnetization is

* Corresponding author. Fax: +1 213 740 4651.
E-mail address: hsulee@usc.edu (H.-L. Lee).

1090-7807/$ - see front matter © 2008 Elsevier Inc. All rights reserved.
doi:10.1016/j.jmr.2008.09.016

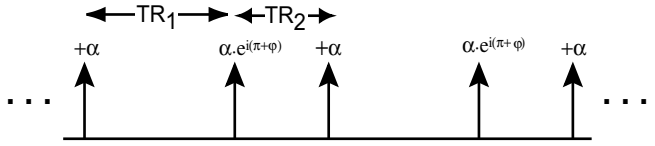

Fig. 1. An alternating TR SSFP sequence. Black arrows represent RF excitation pulses.

alternating between two positions instead of returning to the same place after each excitation.

In the following section, we set $\varphi = 0$ for simplicity, and later will show that the result can be extended to arbitrary φ when $0 \leqslant \varphi < \pi$. Relaxation is neglected since its effects on signal oscillation are not as significant as the direction of the magnetization [4].

2.1. Characterization of the cycle rotation

In order to determine the resulting magnetization after multiple cycles of ATR SSFP sequence, first we need to characterize its cycle-rotation matrix. We define $\mathbf{R}_0$ to be the transition matrix for one full cycle of the alternating TR sequence. When $\mathbf{R}_0$ rotates a magnetization from its position at $TR_1/2$ ($\mathbf{M}_1$) to $TR_2/2$ ($\mathbf{M}_2$) and back to $\mathbf{M}_1$ at the next $TR_1/2$ ($\mathbf{M}_1 = \mathbf{R}_0\mathbf{M}_1$, see Fig. 2), we find $\mathbf{M}_1$ to be the *steady-state* magnetization, which is identical to the axis of $\mathbf{R}_0$ rotation. $\mathbf{R}_0$ can be written as the product of a series of 3×3 orthogonal rotation matrices (all representing right-hand rotations):

$$\mathbf{R}_0 = \mathbf{R}_1 \cdot \mathbf{R}_2 = [\mathbf{R}_z(\theta_1)\mathbf{R}_x(\alpha)\mathbf{R}_z(\theta_2)] \cdot [\mathbf{R}_z(\theta_2)\mathbf{R}_x(-\alpha)\mathbf{R}_z(\theta_1)] \tag{1}$$

where α is the flip angle, $\theta_1(= -\Delta f \cdot \pi \cdot \mathrm{TR}_1)$ and $\theta_2(= -\Delta f \cdot \pi \cdot \mathrm{TR}_2)$ are the magnetization phase offsets due to off-resonance during

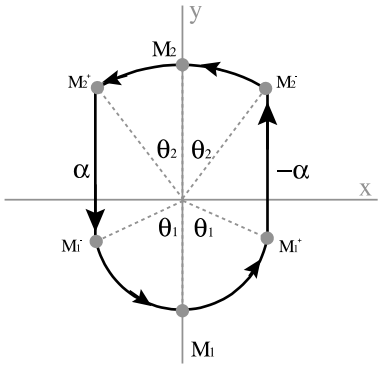

Fig. 2. The steady-state magnetization path of an alternating TR SSFP sequence with $(0, \pi)$ phase-cycling. A full-cycle rotation of a magnetization with resonance offset Δf starts at $\mathbf{M}_1$. It experiences phase offset of $\theta_1(= -\Delta f \cdot 2\pi \cdot \mathrm{TR}_1/2)(\mathbf{M}_1 \to \mathbf{M}_1^+)$, RF excitation of angle $-\alpha(\mathbf{M}_1^+ \to \mathbf{M}_2^-)$, phase offset $\theta_2(= -\Delta f \cdot 2\pi \cdot \mathrm{TR}_2/2)$ and becomes $\mathbf{M}_2$. Then it experiences another phase offset $\theta_2(\mathbf{M}_2 \to \mathbf{M}_2^+)$, excitation $\alpha(\mathbf{M}_2^+ \to \mathbf{M}_1^-)$, phase offset θ_1 and it returns to $\mathbf{M}_1$.

$\mathrm{TR}_1/2$ and $\mathrm{TR}_2/2$, respectively. $\mathbf{R}_1$ and $\mathbf{R}_2$ are the rotation matrices for the first and second half-cycles, that $\mathbf{M}_2 = \mathbf{R}_2\mathbf{M}_1$ and $\mathbf{M}_1 = \mathbf{R}_1\mathbf{M}_2$. By re-writing the above matrices using SU_2 formalism (see Appendix A), we find the rotation axis $\boldsymbol{n}_1(= n_{1x}\hat{i} + n_{1y}\hat{j} + n_{1z}\hat{k}$, without normalization) and rotation angle Ω_1 of $\mathbf{R}_1$ matrix to be

$$\begin{aligned} n_{1x} &= \sin\left(\frac{\alpha}{2}\right)\cos\left(\frac{R\theta}{2}\right) \\ n_{1y} &= \sin\left(\frac{\alpha}{2}\right)\sin\left(\frac{R\theta}{2}\right) \\ n_{1z} &= \cos\left(\frac{\alpha}{2}\right)\sin\left(\frac{\theta}{2}\right) \\ \Omega_1 &= 2\cos^{-1}\left[\cos\left(\frac{\alpha}{2}\right)\cos\left(\frac{\theta}{2}\right)\right] \end{aligned} \tag{2}$$

where $\theta = \theta_1 + \theta_2$ and $R = (\theta_1 - \theta_2)/(\theta_1 + \theta_2)$. Similarly, $\mathbf{R}_2$ has its rotation axis $\boldsymbol{n}_2(= n_{2x}\hat{i} + n_{2y}\hat{j} + n_{2z}\hat{k}$, without normalization) and rotation angle Ω_2 as

$$\begin{aligned} n_{2x} &= -\sin\left(\frac{\alpha}{2}\right)\cos\left(\frac{R\theta}{2}\right) \\ n_{2y} &= \sin\left(\frac{\alpha}{2}\right)\sin\left(\frac{R\theta}{2}\right) \\ n_{2z} &= \cos\left(\frac{\alpha}{2}\right)\sin\left(\frac{\theta}{2}\right) \\ \Omega_2 &= 2\cos^{-1}\left[\cos\left(\frac{\alpha}{2}\right)\cos\left(\frac{\theta}{2}\right)\right] \end{aligned} \tag{3}$$

We then define $\Omega \equiv \Omega_2 = \Omega_1$, where $\Omega \approx 2\cos^{-1}[\cos(\theta/2)] = \theta$ for small α values. $\boldsymbol{n}_1, \boldsymbol{n}_2, \mathbf{M}_1$, and $\mathbf{M}_2$ are plotted in Fig. 3. Note that $\boldsymbol{n}_1$ and $\boldsymbol{n}_2$ are situated in the bisector plane of $\widehat{\mathbf{M}_1\mathbf{M}_2}$ and are symmetric about the y–z-plane, with the norms

$$\begin{aligned} \|\boldsymbol{n}_1\| = \|\boldsymbol{n}_2\| &= [1 - \cos^2(\alpha/2)\cos^2(\theta/2)]^{\frac{1}{2}} = [1 - \cos^2\Omega]^{\frac{1}{2}} \\ &= \sin\Omega. \end{aligned} \tag{4}$$

2.2. Approach to steady-state from thermal equilibrium

Fig. 3a and b shows the projections of the vectors on x–y and y–z-planes, respectively, and Fig. 3c contains the three-dimensional depiction. We define ϕ_1 as the zenith angle between z-axis and $\boldsymbol{n}$ (the projection of $\boldsymbol{n}_1$ and $\boldsymbol{n}_2$ on y–z-plane), and ϕ_2 as the angle between $\boldsymbol{n}$ and $\mathbf{M}_1$ (which is equal to the angle between $\boldsymbol{n}$ and $\mathbf{M}_2$). The values of ϕ_1 and ϕ_2 are determined by the RF flip angles of the current $\mathbf{R}_1$ and $\mathbf{R}_2$ rotation. These two variables indicate the direction of the steady-state magnetizations, hence are essential for the calculation of transient oscillating residues.

Fig. 3 along side with the derivation in Appendix B describes the relation between ϕ_1, ϕ_2, and RF flip angle. Starting from thermal equilibrium (when magnetizations are aligned with z-axis), an initial varying RF sequence $\{\alpha_k\}$ is applied. From Fig. 3b we find that

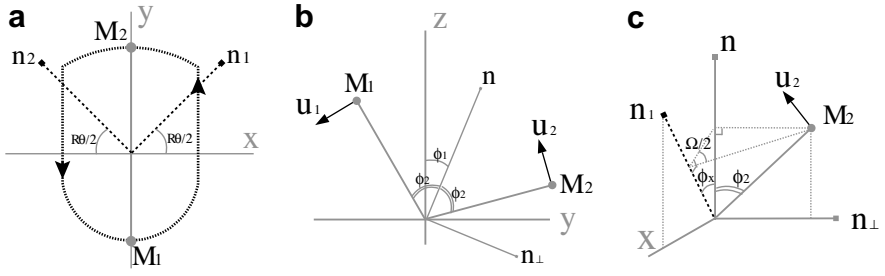

Fig. 3. The relation between $M_1, M_2, \boldsymbol{n}_1$, and $\boldsymbol{n}_2$. (a) 2D plot in x–y-plane. Dotted line represents the magnetization path as in Fig. 2. (b) 2D plot in y–z-plane. ϕ_1 is the angle between z-axis and $\boldsymbol{n}$ (the projection of $\boldsymbol{n}_1$ and $\boldsymbol{n}_2$ on y–z-plane), ϕ_2 is the angle between $\boldsymbol{n}$ and both $\mathbf{M}_1$ and $\mathbf{M}_2$. Vector $\boldsymbol{n}_\perp$ is in the y–z-plane and perpendicular to $\boldsymbol{n}$. (c) 3D plot with three axes being $(x, \boldsymbol{n}, \boldsymbol{n}_\perp)$. ϕ_x is the angle between $\boldsymbol{n}$ and $\boldsymbol{n}_1$ in $(x, \boldsymbol{n})$ plane.

after the k^{th} excitation, when the flip angle α_k is small, the change in ϕ_1 value during this half-cycle (denoted as $\Delta\phi_1(k)$) is proportional to the RF flip angle increment $\Delta\alpha_k(=\alpha_k-\alpha_{k-1})$ that

$$\Delta\phi_1(k)=\Delta\alpha_k\cdot\frac{\sin(R\theta/2)}{2\sin(\theta/2)} \tag{5}$$

From Fig. 3c we also find $\Delta\phi_2(k)$ to be proportional to $\Delta\alpha_k$:

$$\Delta\phi_2(k)=\Delta\alpha_k\cdot\frac{\cos(R\theta/2)}{2\cos(\theta/2)} \tag{6}$$

Please see Appendix B for complete derivations of Eqs. (5) and (6).

2.3. Transient oscillatory residues

We define the oscillatory residue $\boldsymbol{\varepsilon}$ to be the magnetization component perpendicular to its steady-state position. It lies in the $(\boldsymbol{u}_1,\boldsymbol{x})$ plane (perpendicular to $\mathbf{M}_1$) at $TR_1/2$ and in $(\boldsymbol{u}_2,\boldsymbol{x})$ plane (perpendicular to $\mathbf{M}_2$) at $TR_2/2$ (see Fig. 3b). After the k^{th} RF excitation, the new oscillatory residue $\boldsymbol{\varepsilon}_k$ can be calculated by first adding the shift in the steady-state magnetization vector (=the origin of $(\boldsymbol{u},\boldsymbol{x})$ plane) to $\boldsymbol{\varepsilon}_{k-1}$, then apply the Ω rotation. The relation between the oscillatory residues in two consecutive echoes can thus be written as

$$\boldsymbol{\varepsilon}_k=e^{-i\Omega}\left[\boldsymbol{\varepsilon}_{k-1}+\Delta\phi_1(k)|\mathbf{M}|+e^{-i\pi k}\Delta\phi_2(k)|\mathbf{M}|\right] \tag{7}$$

The $e^{-i\pi k}$ term represents the alternating sign of $\Delta\phi_2$ during TR_1 and TR_2.

Defining the phase-shifted oscillatory residue $\epsilon_k=\varepsilon_k\cdot e^{i\Omega k}$ and setting the magnetization magnitude $|\mathbf{M}|=1$, with Eqs. (5) and (6), we find the oscillatory residue ϵ_p after p excitations (p is an even number) to be

$$\epsilon_p=\frac{1}{2}\left[\frac{\sin(R\theta/2)}{\sin(\theta/2)}\sum_{k=1}^{p}\left(e^{i\theta(k-1)}\Delta\alpha_k\right)-\frac{\cos(R\theta/2)}{\cos(\theta/2)}\sum_{k=1}^{p}\left(e^{i(\theta-\pi)(k-1)}\Delta\alpha_k\right)\right] \tag{8}$$

which shows that the oscillatory residue function is a linear combination of the Fourier transforms of the flip angle increment sequence $\{\Delta\alpha_k\}$ (see Appendix C for the complete derivation). Note that when $TR_1=TR_2$, this simplifies to balanced SSFP, and is equivalent to Eq.(24) in Ref. [4]. The preparation sequence for a steady-state sequence with imaging flip angle α' has two constraints, which are $\alpha_0=0$ and $\alpha_p=\alpha'$.

A windowing function $\{w_k\}$ is then chosen as the base flip angle increment sequence for initial preparation. We split $\{w_k\}$ into two separate series of its odd and even elements, multiply them with scalars b_1 and b_2, respectively ($b_1+b_2=1$ in order to meet the $\alpha_p=\alpha'$ constraint). The new flip angle increment sequence becomes $\{b_m w_k\}$ ($m=1$ when k is even, $m=2$ when k is odd), and the oscillatory residue can be re-written as

$$\begin{aligned}\epsilon_p=&\frac{\sin(R\theta/2)}{\sin(\theta/2)}\left[b_1\sum_{k=1}^{p/2}\left(e^{i\theta(2k-1)}w_{2k}\right)+b_2\sum_{k=1}^{p/2}\left(e^{i\theta(2k-2)}w_{2k-1}\right)\right]\\&+\frac{\cos(R\theta/2)}{\cos(\theta/2)}\left[b_1\sum_{k=1}^{p/2}\left(e^{i\theta(2k-1)}w_{2k}\right)-b_2\sum_{k=1}^{p/2}\left(e^{i\theta(2k-2)}w_{2k-1}\right)\right]\end{aligned} \tag{9}$$

We can then optimize b_1 and b_2 for any resonance offset by minimizing $|\epsilon_p|$ at $\theta\sim\theta_0=-\Delta f\cdot\pi\cdot(TR_1+TR_2)$. From Eq. (9) we know that $|\epsilon_p|_{\theta\sim\theta_0}$ has its minimum when

$$\begin{aligned}|\epsilon_p|_{\theta\sim\theta_0}&=\left[\frac{\sin(R\theta/2)}{\sin(\theta/2)}(b_1+b_2)+\frac{\cos(R\theta/2)}{\cos(\theta/2)}(b_1-b_2)\right]\cdot\mathscr{F}\{w_{2k-1}\}=0\\&=\frac{\tan(R\theta/2)}{\tan(\theta/2)}(b_1+b_2)+(b_1-b_2)\end{aligned} \tag{10}$$

Considering a wideband SSFP sequence (alternating TR SSFP with $(0,\pi)$ phase-cycling) [11], for the center of passband $\theta\sim0$, the optimized $b_1/b_2\approx(1-R)/(1+R)=TR_2/TR_1$. Fig. 4a shows an optimized eight-step Kaiser–Bessel windowed flip angle increment sequence $\{\Delta\alpha_k\}$, that its elements form an alternatively scaled Kaiser–Bessel windowing function. The actual flip angle ramp for the initial preparation is shown in Fig. 4b.

Numerical simulations of different choices of window function $\{w_k\}$ and scalars (b_1,b_2) were performed for a wideband SSFP sequence with $p=8$ (four full-cycles). Fig. 4c shows the oscillatory

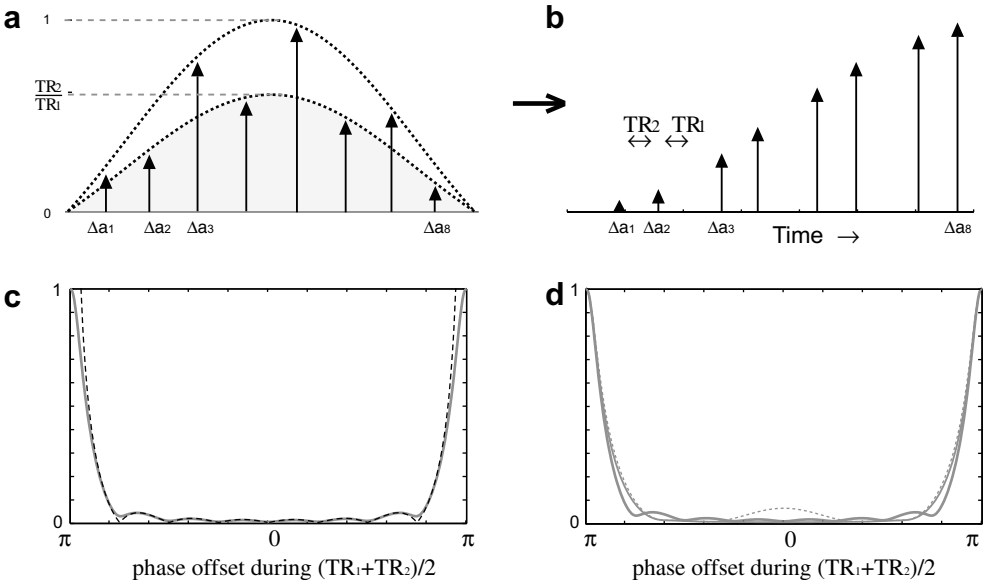

Fig. 4. Wideband SSFP sequence: (a) an RF flip angle increment sequence $\{\Delta\alpha_k\}$ designed using Kaiser–Bessel windowing functions with optimized ratios. (b) The actual RF ramp sequence calculated using values in (a), that $\alpha_k=\sum_{n=1}^{k}\Delta\alpha_n$. (c) The absolute value of simulated oscillatory residues after an optimized 8-step linear ramp preparation. Grey solid line represents the true residue values obtained using matrix rotation, black dashed line represents the result given by Eq. (9). (d) True residue values after 8-step linear ramp and Kaiser–Bessel windowed ramp preparation. Black solid line: optimized Kaiser–Bessel window ($\beta=3$), grey dashed line: Kaiser–Bessel window ($\beta=3$) with $b_1=b_2=0.5$, grey solid line: linear ramp.

residues after linear ramps (ramps based on a rectangular window, i.e. the flip angle increments are constant) with optimized b_1, b_2. The solid line represents the true oscillatory residue values calculated using four $\mathbf{R}_0$ matrix rotations, and dotted line represents the approximated values obtained from Eq. (9). The approximated and true $|\epsilon_p|$ functions are in close agreement within the passband. Fig. 4d shows true oscillatory residues after a linear ramp (optimized b_1, b_2) and Kaiser–Bessel windowed [13] ramps (flip angle increments forms a Kaiser–Bessel window) with both optimized (b_1, b_2) and $b_1 = b_2 = 0.5$. The Kaiser–Bessel window was chosen because its shape can be flexibly modified by adjusting one control parameter β, and because it provides a near-optimal solution [14]. The black solid line represents the Kaiser–Bessel windowed ramp with optimized b_1 and b_2, which shows the best oscillatory residue attenuation among the three methods.

2.4. General model for ATR SSFP sequences

This approach can be generalized to alternating TR sequences with an RF phase-cycling of $(0, \pi + \varphi), 0 \leqslant \varphi < \pi$ by writing down the new full-cycle rotation matrix $\mathbf{R}'_0$ as

$$\begin{aligned}\mathbf{R}'_0 &= \mathbf{R}'_1 \cdot \mathbf{R}'_2 \\ &= [\mathbf{R}_z(\theta_1)\mathbf{R}_x(\alpha)\mathbf{R}_z(\theta_2)] \cdot [\mathbf{R}_z(\theta_2)\mathbf{R}_z(\varphi)\mathbf{R}_x(-\alpha)\mathbf{R}_z(-\varphi)\mathbf{R}_z(\theta_1)] \\ &= [\mathbf{R}_z(\theta'_1)\mathbf{R}_x(\alpha)\mathbf{R}_z(\theta'_2)] \cdot [\mathbf{R}_z(\theta'_2)\mathbf{R}_x(-\alpha)\mathbf{R}_z(\theta'_1)] \end{aligned} \quad (11)$$

which has the same form as $\mathbf{R}_0$ in Eq. (1), with $\theta'_1 = \theta_1 - \varphi/2, \theta'_2 = \theta_2 + \varphi/2$. Therefore the oscillatory residue can be obtained by substituting $R\theta$ in Eq. (9) with $(R\theta - \varphi)$:

$$\begin{aligned}\epsilon_p = &\frac{\sin((R\theta-\varphi)/2)}{\sin(\theta/2)}\left[b_1\sum_{k=1}^{p/2}\left(e^{i\theta(2k-1)}w_{2k}\right) + b_2\sum_{k=1}^{p/2}\left(e^{i\theta(2k-2)}w_{2k-1}\right)\right] \\ &+\frac{\cos((R\theta-\varphi)/2)}{\cos(\theta/2)}\left[b_1\sum_{k=1}^{p/2}\left(e^{i\theta(2k-1)}w_{2k}\right) - b_2\sum_{k=1}^{p/2}\left(e^{i\theta(2k-2)}w_{2k-1}\right)\right]\end{aligned} \quad (12)$$

and the relation between optimized scalars b_1 and b_2 becomes

$$\left(1+\frac{\tan[(R\theta_0-\varphi)/2]}{\tan(\theta_0/2)}\right)\cdot b_1 = \left(1-\frac{\tan[(R\theta_0-\varphi)/2]}{\tan(\theta_0/2)}\right)\cdot b_2 \quad (13)$$

For example, an FS-ATR SSFP sequence [10] with $TR_2 = TR_1/3$ and $(0, \frac{3}{4}\pi)$ RF phase-cycling has center of passband (water frequency) at $\theta_0 = -\pi/2$ (omitting the RF phase increment to shift water to $\theta = 0$, for simplicity). Using Eq. (13), the optimized b_1 and b_2 for water frequency will be

$$b_1 = b_2 = 0.5$$

We can also optimize b_1 and b_2 for the center of the stopband (fat frequency), which is at $\theta_0 = \pi/2$, and obtain

$$b_1 = 0, \quad b_2 = 1$$

Flip angle increments and amplitudes in the ATR SSFP preparation scheme designed using Kaiser–Bessel window and the optimized (b_1, b_2) values for the water band are shown in Fig. 5a and b.

Numerical simulations of different $\{w_k\}$ and (b_1, b_2) were also performed for this sequence with $p = 8$ (four full-cycles), and the results are shown in Fig. 5. In Fig. 5c, solid and dotted lines represent the true oscillatory residue values after four $\mathbf{R}'_0$ rotations and the approximated values from Eq. (12), respectively. The approximated and true $|\epsilon_p|$ functions are in close agreement except for frequencies around the null bands of the ATR SSFP. Fig. 5d shows true oscillatory residues after a linear ramp ($b_1 = b_2 = 0.5$, optimized for water) and Kaiser–Bessel windowed [13] ramps ($b_1 = b_2 = 0.5$, optimized for water and $b_1 = 0, b_2 = 1$, optimized for fat). The black solid line represents the Kaiser–Bessel windowed ramp with b_1 and b_2 optimized for water, which shows the best oscillatory residue attenuation within the water passband. Grey dotted line represents Kaiser–Bessel windowed ramp with b_1 and b_2 optimized for fat, and this sequence suppresses oscillatory residues better inside the fat-band.

3. Experimental methods

Experiments were performed on a Signa Excite HD 3T scanner (GE Healthcare, Waukesha, WI) with a single-channel head coil.

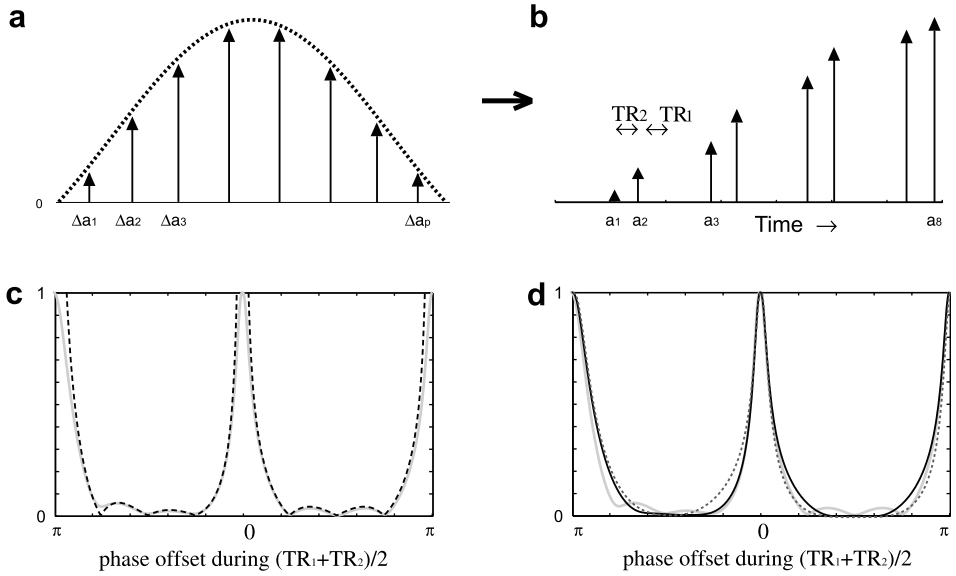

Fig. 5. Fat-suppressed ATR SSFP sequence: (a) an RF flip angle increment sequence $\{\Delta\alpha_k\}$ designed using Kaiser–Bessel windowing functions with (b_1, b_2) optimized for water band. (b) The actual RF ramp sequence calculated using values in (a), that $\alpha_k = \sum_{n=1}^{k}\Delta\alpha_n$. (c) The absolute value of simulated oscillatory residues after an optimized eight-step linear ramp preparation. Grey solid line represents the true residue values obtained using matrix rotation, black dashed line represents the result given by Eq. (9). (d) True residue values after 8-step linear ramp and Kaiser–Bessel windowed ramp preparation. Black solid line: Kaiser–Bessel window ($\beta = 3$) optimized for water band, grey dotted line: Kaiser–Bessel window ($\beta = 3$) optimized for fat band, grey solid line: linear ramp optimized for water band.

To measure the transient signal of different resonant frequencies, a linear shim was used to generate a frequency gradient in a uniform spherical ball phantom ($T_1/T_2 = 150/35$). A pulse sequence was designed to wait for thermal equilibrium, apply an eight-step initial preparation sequence, and then acquire the same phase encode for 64 full-cycles. The process repeats for all the phase encoding steps, so that a complete image can be reconstructed for each imaging TR after starting from thermal equilibrium. Finally, we extract one line from each image to plot the spectral profile evolution during the approach to steady state.

Experimentally measured transient signals were compared with Bloch simulations in MATLAB (Mathworks, Inc., South Natick, MA). Three types of initial preparation were considered: dummy-cycles, linear ramp and Kaiser–Bessel ramp preparations (b_1, b_2 optimized for water). All preparations consisted of eight pulses (four full-cycles) and were 28ms in length. Two alternating TR SSFP sequences were considered: wideband SSFP and FS-ATR SSFP. The prescribed flip angle was 45° in all scans.

Phantom imaging with eight-step initial preparations and centric phase-encoding ordering was also performed for wideband SSFP and FS-ATR SSFP sequences to observe the artifacts caused by transient signal oscillation. Three ramp types were used: dummy cycles, linear ramp, and Kaiser–Bessel windowed ramp. Shim gradients were applied to create a ±25 Hz off-resonance span in the uniform ball phantoms. In wideband SSFP experiments the ramps were optimized for the center of passband ($\Delta f = 0$). Ramps optimized for different frequencies were tested in FS-ATR SSFP scans. Two phantoms were imaged with their resonant frequencies centered at water (pass band) and fat (stop band).

4. Results

Fig. 6 contains the simulated and measured transient signals from a uniform phantom, as functions of number of cycles and resonant frequency. The experimental measurements show good agreement with the simulation. The measured spectral profiles are smoother compared to simulated ones because the real phantom reflects a continuous intra-voxel frequency distribution, whereas the simulation is discretely sampled in frequency. This frequency distribution also facilitates the decay of signal oscillation in experiments compared to simulations. Grey arrows indicate the point when central dips [11] become visible. The formation of a central dip in the spectral profile is related to magnetization relaxation, and it begins to form after the sequence reaches a constant flip angle. Hence, the two ramp-up preparation schemes result in a delayed appearance of the dip compared to dummy-cycle preparation.

Initial preparations consisted of eight RF pulses (four full cycles), were 28 ms in length, and consisted of either dummy cycles, linear ramp, or Kaiser–Bessel ramp optimized for the center of the water band. Tables 1 and 2 contain the averaged measured magnitude of oscillation over half of the passband and

Table 1
Measured signal oscillation magnitude during the first 10 cycles of wideband SSFP, for three initial preparation schemes

	Dummy cycles	Linear	Kaiser–Bessel
Center passband (%)	18.7	4.6	1.8

Values are averaged over half the passband.

Table 2
Measured signal oscillation magnitude during the first 10 cycles of FS-ATR SSFP, for three initial preparation schemes

	No preparation	Linear	Kaiser–Bessel
Water band (%)	41.3	1.0	0.4
Fat band (%)	48.6	9.4	8.3

Values are averaged over half the water band and fat band.

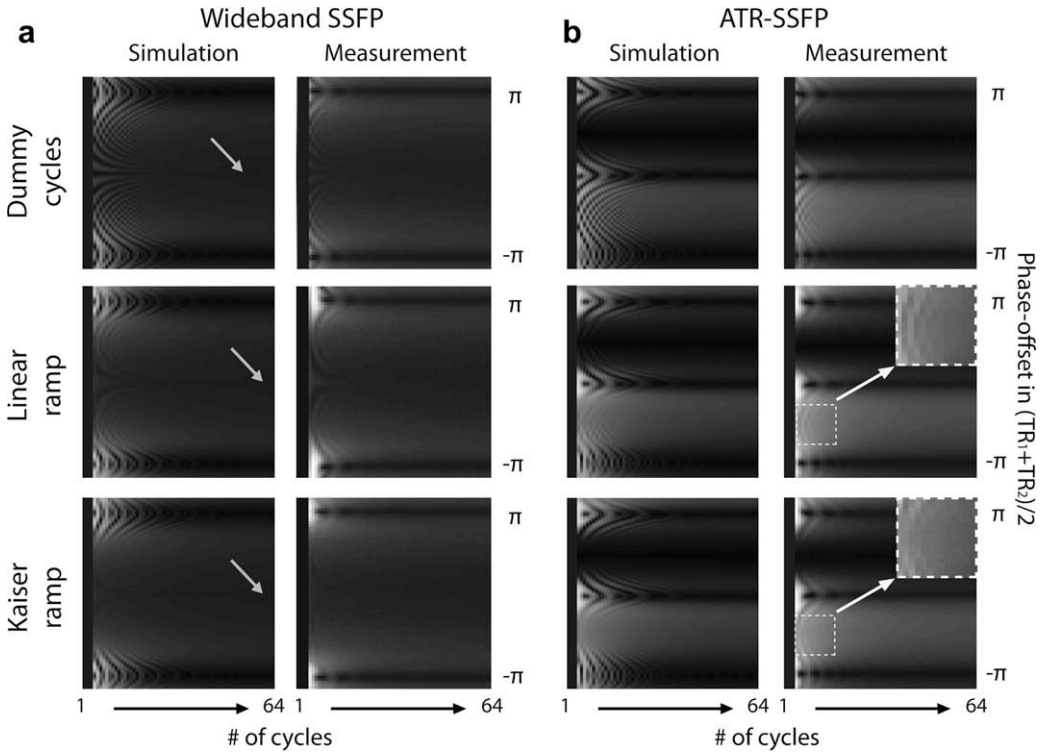

Fig. 6. Simulated and measured transient signals of a ball phantom after different preparation methods. (a) Wideband SSFP, grey arrows indicate when the central dips appear. (b) FS-ATR SSFP. The experimental measurements show good agreement with the simulation. Kaiser–Bessel windowed ramp significantly reduced the transient signal fluctuation.

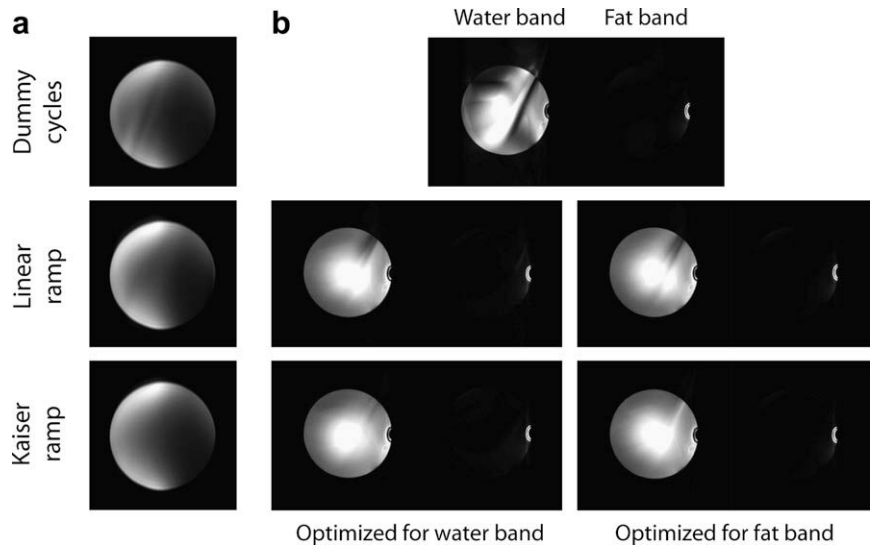

Fig. 7. Alternating TR SSFP phantom images after different preparation methods. Eight-step preparation was used for all the scans. Images obtained with Kaiser–Bessel windowed ramp show better image uniformity and reduced artifacts. (a) Wideband SSFP images. Ramps were optimized for the center of passband where $\Delta f = 0$. (b) FS-ATR SSFP images. Resonant frequencies of the two phantoms were centered at water band (pass band) and fat band (stop band), with a ± 25 *Hz* span. Ramps optimized for water (left column) and fat (right column) bands were both tested.

stopband in the first 10 imaging cycles after different preparation schemes. Table values reflect the magnitude of oscillation relative to the steady-state signal amplitude. In wideband SSFP (Table 1), linear ramp reduced the oscillation from 18.7% to 4.6%, and Kaiser–Bessel ramp preparation further reduced it to 1.8% (the percentage represents the amount of oscillation compared to steady-state magnitude). In FS-ATR SSFP (Table 2), linear and Kaiser–Bessel ramps optimized for water resonant frequency reduced the amount of oscillation in water band from 41.3% to 1.0% and 0.4%, respectively. The oscillation reduction in fat band was from 48.6% to 9.4% (linear ramp) and 8.3% (Kaiser–Bessel ramp).

Fig. 7 shows the actual images obtained after different eight-step initial preparation schemes. Images obtained with Kaiser–Bessel windowed ramp have significantly reduced artifacts in both sequences. In FS-ATR SSFP images (Fig. 7b), initial ramps with different (b_1, b_2) scalars show slightly more uniform signal and less artifact along the phase-encoding (vertical) direction, around the frequency bands they are optimized for. However, the visible differences are subtle.

5. Discussion

Simulations and phantom experiments demonstrate ATR SSFP imaging with reduced signal oscillation using optimized Kaiser–Bessel windowed ramp preparation, compared to dummy-cycles and linear ramp preparation. The preparation scheme can be easily modified to minimize oscillatory residue at the desired resonant frequency using Eq. (12), and only a simple recalculation is needed when changing the length of preparation. This method is expected to be robust in the presence of B_1^+ variation because it only relies on relative flip angle amplitudes.

The Fourier relation between RF amplitude increments and the amount of oscillatory residue is based on the assumption that half of the imaging flip angle $\alpha/2$ is small. As the flip angle becomes larger, actual oscillatory residues start to deviate from Eq. (8). Nevertheless, note that the small angle approximation $(\tan(\alpha/2) \approx \alpha/2)$ used in Eqs. (5) and (6) only has a 10% error even when the value of α is as high as 60°. This more than covers the flip angle range typically used in ATR SSFP imaging.

Relaxation effects are neglected in our model, due to the fact that T_1 and T_2 has little effect on the magnetization direction during initial preparation [4]. In reality, relaxation would result in a decreasing magnetization length which would introduce an additional smooth transient signal weighting in k-space, which is not expected to cause substantial deviation from this model.

In this work, the coefficients b_1 and b_2 are optimized solely with respect to the center of passband, independent of the chosen windowing function. Therefore, the ramps may become slightly less effective as the amount of off-resonance increases. For this reason a Kaiser–Bessel windowing function is preferred since it has peak concentration around its pass band center and good attenuation in the side-lobes [14], thus the oscillatory residue can remain suppressed for a wide range of frequencies. As Fig. 7 shows, Kaiser–Bessel windowed ramps optimized for water frequency still perform well in the fat band, and the same for the opposite case. Further optimization using numerical calculation over a frequency band is possible, in which case the spectral response of the windowing function and subject off-resonance characteristic will also become factors in the decision of b_1 and b_2.

6. Conclusions

We have developed a model for transient magnetization in alternating TR SSFP. Initial preparation sequences can be designed using a two-step process: first choose a windowing function (preferably a Kaiser–Bessel window), then optimize the (b_1, b_2) parameters by minimizing the oscillatory residue given in Eq. (12). Kaiser–Bessel windowed ramps with scaling factors optimized for wideband SSFP and FS-ATR SSFP were tested in phantom experiments, and the results showed signifiant reduction of transient signal oscillation in both cases. The proposed design can be applied to any combination of repetition times and RF phase-cycling. It is easy to implement, and actively reduces oscillatory residues during the transient approach to steady state.

Appendix A

Using SU_2 formalism, $\mathbf{R}_1$ (representing the rotation from $\mathbf{M}_2$ to $\mathbf{M}_1$) can be re-written as a 2×2 spinor matrix $\mathbf{Q}_1$:

$$\mathbf{Q}_1 = \mathbf{Q}_z(\theta_1)\mathbf{Q}_x(\alpha)\mathbf{Q}_z(\theta_2)$$
$$= \begin{bmatrix} e^{-i\theta_1/2} & 0 \\ 0 & e^{i\theta_1/2} \end{bmatrix} \cdot \begin{bmatrix} \cos\left(\frac{\alpha}{2}\right) & -i\sin\left(\frac{\alpha}{2}\right) \\ -i\sin\left(\frac{\alpha}{2}\right) & \cos\left(\frac{\alpha}{2}\right) \end{bmatrix} \cdot \begin{bmatrix} e^{-i\theta_2/2} & 0 \\ 0 & e^{i\theta_2/2} \end{bmatrix}$$
$$= \cos\left(\frac{\alpha}{2}\right)\cos\left(\frac{\theta}{2}\right)\cdot\mathbf{I} - i\begin{bmatrix} \cos\left(\frac{\alpha}{2}\right)\sin\left(\frac{\theta}{2}\right) & \sin\left(\frac{\alpha}{2}\right)e^{-iR\theta/2} \\ \sin\left(\frac{\alpha}{2}\right)e^{iR\theta/2} & -\cos\left(\frac{\alpha}{2}\right)\sin\left(\frac{\theta}{2}\right) \end{bmatrix}$$

where $\theta = \theta_1 + \theta_2$ and $R = (\theta_1 - \theta_2)/(\theta_1 + \theta_2)$. As described in Ref. [8], an SU_2 matrix $\mathbf{Q}$ can have its rotation axis $\boldsymbol{n}(= n_x\hat{i} + n_y\hat{j} + n_z\hat{k})$ and rotation angle Ω extracted directly from the matrix elements, that

$$\mathbf{Q} = \cos\left(\frac{\Omega}{2}\right)\cdot\mathbf{I} - i\cdot\sin\left(\frac{\Omega}{2}\right)\cdot\begin{bmatrix} n_z & n_x - in_y \\ n_x + in_y & -n_z \end{bmatrix}$$

$\mathbf{I}$ is the identity matrix. Thus for matrix $\mathbf{Q}_1$ we find

$$n_{1x} = \sin\left(\frac{\alpha}{2}\right)\cos\left(\frac{R\theta}{2}\right)$$
$$n_{1y} = \sin\left(\frac{\alpha}{2}\right)\sin\left(\frac{R\theta}{2}\right)$$
$$n_{1z} = \cos\left(\frac{\alpha}{2}\right)\sin\left(\frac{\theta}{2}\right)$$
$$\Omega_1 = 2\cos^{-1}\left[\cos\left(\frac{\alpha}{2}\right)\cos\left(\frac{\theta}{2}\right)\right]$$

The same approach can be applied to $\mathbf{R}_2$ rotation to get the another 2×2 matrix $\mathbf{Q}_2$:

$$\mathbf{Q}_2 = \mathbf{Q}_z(\theta_2)\mathbf{Q}_x(-\alpha)\mathbf{Q}_z(\theta_1)$$
$$= \begin{bmatrix} e^{-i\theta_2/2} & 0 \\ 0 & e^{i\theta_2/2} \end{bmatrix} \cdot \begin{bmatrix} \cos\left(\frac{\alpha}{2}\right) & i\sin\left(\frac{\alpha}{2}\right) \\ i\sin\left(\frac{\alpha}{2}\right) & \cos\left(\frac{\alpha}{2}\right) \end{bmatrix} \cdot \begin{bmatrix} e^{-i\theta_1/2} & 0 \\ 0 & e^{i\theta_1/2} \end{bmatrix}$$
$$= \cos\left(\frac{\alpha}{2}\right)\cos\left(\frac{\theta}{2}\right) - i\begin{bmatrix} \cos\left(\frac{\alpha}{2}\right)\sin\left(\frac{\theta}{2}\right) & -\sin\left(\frac{\alpha}{2}\right)e^{iR\theta/2} \\ -\sin\left(\frac{\alpha}{2}\right)e^{-iR\theta/2} & -\cos\left(\frac{\alpha}{2}\right)\sin\left(\frac{\theta}{2}\right) \end{bmatrix}$$

and its rotation axis $\boldsymbol{n}_2(= n_{2x}\hat{i} + n_{2y}\hat{j} + n_{2z}\hat{k})$ and rotation angle Ω_2 are

$$n_{2x} = -\sin\left(\frac{\alpha}{2}\right)\cos\left(\frac{R\theta}{2}\right)$$
$$n_{2y} = \sin\left(\frac{\alpha}{2}\right)\sin\left(\frac{R\theta}{2}\right)$$
$$n_{2z} = \cos\left(\frac{\alpha}{2}\right)\sin\left(\frac{\theta}{2}\right)$$
$$\Omega_2 = 2\cos^{-1}\left[\cos\left(\frac{\alpha}{2}\right)\cos\left(\frac{\theta}{2}\right)\right] = \Omega_1$$

Appendix B

In Fig. 3b we define ϕ_1 as the angle between z-axis and $\boldsymbol{n}$, and observe that

$$\tan\phi_1 = \frac{n_{1y}}{n_{1z}} = \frac{n_{2y}}{n_{2z}} = \frac{\sin(\alpha/2)\sin(R\theta/2)}{\cos(\alpha/2)\sin(\theta/2)} = \tan\left(\frac{\alpha}{2}\right)\cdot\frac{\sin(R\theta/2)}{\sin(\theta/2)}$$

For small $\alpha/2$ values we have $\tan(\alpha/2)\approx\alpha/2$, therefore

$$\phi_1 \approx \alpha\cdot\frac{\sin(R\theta/2)}{2\sin(\theta/2)}$$

Considering a sequence of excitations with RF flip angles $\{\alpha_k\}$, the change in ϕ_1 value after the k^{th} excitation can be expressed as

$$\Delta\phi_1(k) = \phi_1(k) - \phi_1(k-1) = [\alpha_k - \alpha_{k-1}]\cdot\frac{\sin(R\theta/2)}{2\sin(\theta/2)}$$
$$= \Delta\alpha_k\cdot\frac{\sin(R\theta/2)}{2\sin(\theta/2)}.$$

Defining ϕ_2 as the angle between $\boldsymbol{n}$ and both $\mathbf{M}_1$ and $\mathbf{M}_2$, and plotting $\mathbf{M}_1, \mathbf{M}_2, \boldsymbol{n}_1$ and $\boldsymbol{n}_2$ in 3D space (Fig. 3c), we find

$$\mathbf{M}_2\cdot\cos\phi_2\cdot\sin\phi_x\cdot\tan\left(\frac{\Omega}{2}\right) = \mathbf{M}_2\cdot\sin\phi_2$$

Solving for ϕ_2, we have

$$\tan\phi_2 = \sin\phi_x\cdot\tan\left(\frac{\Omega}{2}\right) = \frac{|n_{1x}|}{\|\boldsymbol{n}_1\|}\cdot\frac{\sin(\Omega/2)}{\cos(\Omega/2)} = \frac{\sin(\alpha/2)}{\cos(\alpha/2)}\cdot\frac{\cos(R\theta/2)}{\cos(\theta/2)}$$
$$= \tan\left(\frac{\alpha}{2}\right)\cdot\frac{\cos(R\theta/2)}{\cos(\theta/2)}$$

Again we apply small-α approximation and obtain

$$\phi_2 \approx \alpha\cdot\frac{\cos(R\theta/2)}{2\cos(\theta/2)}$$

Hence the change in ϕ_2 value after the k^{th} excitation is

$$\Delta\phi_2(k) = \phi_2(k) - \phi_2(k-1) = [\alpha_k - \alpha_{k-1}]\cdot\frac{\cos(R\theta/2)}{2\cos(\theta/2)}$$
$$= \Delta\alpha_k\cdot\frac{\cos(R\theta/2)}{2\cos(\theta/2)}$$

The above equations indicate that for spins of a certain resonant frequency, the amounts of increment in ϕ_1 and ϕ_2 is proportional to the amount of RF flip angle increment $\Delta\alpha$.

Appendix C

Multiplying $e^{i\Omega k}$ to both side of Eq. (7), we obtain a phase-shifted form (ϵ_k) of the oscillatory residue that

$$\epsilon_k = e^{i\Omega k}\boldsymbol{\varepsilon}_k = e^{i\Omega(k-1)}\boldsymbol{\varepsilon}_{k-1} + e^{i\Omega(k-1)}\left[\Delta\phi_1(k) + e^{-i\pi k}\Delta\phi_2(k)\right]$$
$$= \epsilon_{k-1} + e^{i\Omega(k-1)}\frac{\sin(R\theta/2)}{2\sin(\theta/2)}\cdot\Delta\alpha_k - e^{i(\Omega-\pi)(k-1)}\frac{\cos(R\theta/2)}{2\cos(\theta/2)}\cdot\Delta\alpha_k \quad (C.1)$$

Using the fact that when the sequence first starts from thermal equilibrium, $\varepsilon_0 = \epsilon_0 = 0$ and $\Omega\approx\theta$, the oscillatory residue ϵ_p after p excitations (p is an even number) can be calculated by summing up the last two terms in Eq. (C.1):

$$\epsilon_p = \frac{1}{2}\left[\frac{\sin(R\theta/2)}{\sin(\theta/2)}\sum_{k=1}^{p}\left(e^{i\theta(k-1)}\Delta\alpha_k\right) - \frac{\cos(R\theta/2)}{\cos(\theta/2)}\sum_{k=1}^{p}\left(e^{i(\theta-\pi)(k-1)}\Delta\alpha_k\right)\right]$$

which suggests the Fourier relation between ϵ_p and $\{\Delta\alpha_k\}$: the first term is the Fourier transform of $\{\Delta\alpha_k\}$ multiplied by a function of θ; the second term is the same Fourier transform shifted by π and multiplied by another function of θ.

References

[1] H.Y. Carr, Steady-state free precession in nuclear magnetic resonance, Phys. Rev. 112 (1958) 1693–1701.
[2] M. Deimling, O. Heid, Magnetization prepared true FISP imaging, in: Proceedings of the Second Annual Meeting of SMR, San Francisco, 1994, p. 495.
[3] O. Heid, True FISP cardiac fluoroscopy, in: Proceedings of the Fifth Annual Meeting of ISMRM, Vancouver, 1997, p. 320.
[4] P. Le Roux, Simplified model and stabilization of SSFP sequences, J Magn. Reson. 163 (1) (2003) 23–37.
[5] A. Messiah, Quantum Mechanics, Dover, New York, 2000.
[6] E.T. Jaynes, Matrix treatment of nuclear induction, Phys. Rev. 98 (4) (1955) 1099–1105.
[7] A.L. Bloom, Nuclear induction in inhomogeneous fields, Phys. Rev. 98 (4) (1955) 1105–1111.
[8] J. Pauly, P. Le Roux, D. Nishimura, A. Macovski, Parameter relations for the Shinnar–Le Roux selective excitation pulse design algorithm, IEEE Trans. Med. Imaging 10 (1) (1991) 53–65.
[9] B.A. Hargreaves, S.S. Vasanawala, J.M. Pauly, D.G. Nishimura, Characterization and reduction of the transient response in steady-state MR imaging, Magn. Reson. Med. 46 (1) (2001) 149–158.
[10] J. Leupold, J. Hennig, K. Scheffler, Alternating repetition time balanced steady state free precession, Magn. Reson. Med. 55 (2006) 557–565.

[11] K.S. Nayak, H.-L. Lee, B.A. Hargreaves, B.S. Hu, Wideband SSFP: alternating repetition time balanced steady state free precession with increased band spacing, Magn. Reson. Med. 58 (5) (2007) 931–938.
[12] T. Cukur, B.A. Hargreaves, D.G. Nishimura, Reduction of the transient oscillations in alternating-TRSSFP, in: Proceedings of the 15th Annual Meeting of ISMRM, Berlin, 2007, p. 3447.
[13] J.F. Kaiser, Non recursive digital filter design using the i0-sinh window function, in: Proceedings 1974 IEEE International Symposium on Circuits Systems, 1974, pp. 20–23.
[14] A.V. Oppenheim, R.W. Schafer, J.R. Buck, Discrete-Time Signal Processing, Prentice-Hall, Upper Saddle River, NJ, 1999.